JPhys Energy

PURPOSE-LED
PUBLISHING™

**PAPER** • **OPEN ACCESS**

# Optical and charge transport properties of methylammonium versus triple-cation lead halide perovskites: a combined theoretical and experimental study

To cite this article: Adriana Pecoraro *et al* 2025 *J. Phys. Energy* **7** 035004

IOP Publishing J. Phys. Energy 7 (2025) 035004 https://doi.org/10.1088/2515-7655/adc837

Journal of Physics: Energy

CrossMark

OPEN ACCESS

RECEIVED
9 January 2025

REVISED
24 March 2025

ACCEPTED FOR PUBLICATION
1 April 2025

PUBLISHED
15 April 2025

**PAPER**

# Optical and charge transport properties of methylammonium versus triple-cation lead halide perovskites: a combined theoretical and experimental study

**Adriana Pecoraro**[1,*], **Francesca Fasulo**[1], **Carmen Serpico**[2,3], **Gennaro V Sannino**[2,3], **Lucia V Mercaldo**[3], **Paola Delli Veneri**[3], **Michele Pavone**[2] and **Ana Belén Muñoz-García**[1]

[1] Department of Physics 'E. Pancini', University of Naples Federico II, Napoli, Italy
[2] Department of Chemical Sciences, University of Naples Federico II, Napoli, Italy
[3] Italian National Agency for New Technologies, Energy and Sustainable Economic Development (ENEA), Portici Research Center, Portici (Na), Italy
* Author to whom any correspondence should be addressed.

**E-mail:** adriana.pecoraro@unina.it

**Keywords:** perovskites, dielectric function, charge transport

Supplementary material for this article is available online

## Abstract

We investigate the optical and transport properties of two widely used perovskite materials for solar cells, methylammonium lead iodide (MAPI) and triple-cation perovskite (TriLHP), using first-principles calculations. Our theoretical results, supported by ellipsometry measurements, show that MAPI exhibits stronger dielectric screening and better absorption characteristics, which could contribute to enhanced defect tolerance and less sensitivity to light intensity fluctuations. In contrast, TriLHP demonstrates a lighter electron effective mass, attributed to halogen mixing and octahedral distortions, potentially improving electron mobility. We also estimate the exciton binding energy and radius for both materials, confirming their behavior as Wannier–Mott excitons. These findings provide critical insights into the material properties that govern the performance of perovskite solar cells.

## 1. Introduction

Metal halide perovskites have rapidly emerged in the photovoltaic scenario due to their excellent optoelectronic properties, such as high absorption coefficients, optimal bandgap, defect tolerance and long charge carrier lifetimes, that have been key to their success as main component materials for photovoltaic cells [1]. Efforts to maximize the efficiency of solar cells made from methylammonium lead iodide (MAPI) have taken multiple approaches. These include optimizing both device and material fabrication [2], modifying molecules and replacing cations [3], and identifying the most effective electron and hole transport materials [4–11]. Given their general formula $ABX_3$, perovskite materials exhibit a high compositional versatility provided that their structural stability is preserved, as predicted by the Goldschmidt's tolerance factor based on anion/cation radii ratios [12]. The choice of A is broad from inorganic ($Cs^+$, $Rb^+$) to organic cations (MA, FA, etc.) whereas the divalent cation in B is generally $Pb^{2+}$ [13], while recent efforts toward non-toxic lead-free perovskites has been focusing on $Sn^{2+}$ [14]. To date the best perovskite solar cells (PSCs) rely on complex formulations with double (Cs/FA) and triple (MA/FA/Cs) cations and mixed halides (I/Br), in which the presence of a small amount of Cs improves the crystallinity and fabrication reproducibility [3]. Substantial research efforts are dedicated to the exceptional optical and photoconversion characteristics of these lead halide perovskites with different compositions, which contribute to the high performance of these solar cells. These investigations are crucial not only for fundamental theoretical understandings, but also for providing valuable insights for further advancements in PSC technology [15].

Hybrid organic/inorganic perovskites, despite their nature, tend to exhibit optoelectronic properties that closely resemble those of inorganic materials, with the organic component primarily influencing the structural arrangement and overall stability of the material. However, the organic cation is not merely passive; its orientation can significantly affect the crystal structure, which, in turn, influences the electronic properties. The interplay between their organic and inorganic features shapes the material's behavior, impacting on the dielectric features and transport properties that affect the final photovoltaic efficiency.

In halide perovskites, the primary charge carriers are conduction electrons and holes generated by photoexcitation. These carriers can pair via electrostatic interaction to form quasiparticles known as excitons. Consequently, the effective masses of these charge carriers and the exciton binding energy are crucial factors in assessing the material's suitability in solar cells. From an application perspective, the exciton binding energy is crucial for determining device performance since comparing this value with the thermal energy ($kT = 25$ meV at 300 K) reveals whether photo-generated carriers will dissociate naturally.

Numerous studies have explored the dielectric properties of halide perovskites from both experimental and theoretical perspectives. For MAPI, Lin *et al* measured its optical constants and dielectric function, using these to infer exciton behavior. Löper *et al* [16] employed spectroscopic ellipsometry (SE) and spectrophotometry to examine the dielectric function of MAPI thin films, while another study analyzed temperature-dependent polarization and dielectric properties to investigate ferroelectricity in MAPI [17]. The paper by Besra *et al* [18] investigates the effect of the defect density on the dielectric features of MAPI. On the theoretical side, Srikanth *et al* [19] used dispersion-corrected density functional theory (DFT) to study how A-cation size and type influence lattice structures, stability, and electronic polarization in perovskite and non-perovskite phases of $APbI_3$, providing insights into intrinsic instability and comparing optical dielectric constants with experimental data. Additionally, a combined theoretical and experimental approach, incorporating advanced relativistic quasi-particle self-consistent GW calculations, has been used to investigate the optical properties of methylammonium lead perovskites [20]. Some experimental studies targeted to the assessment of the dielectric profile of the triple cation formulation. The study carried out by Hossain *et al* highlights that the lower dielectric relaxation time constant in CsFAMA-based PSCs compared to MAPI-based PSCs, linked to a lower dielectric constant, reveals the influence of monovalent cations on dielectric properties, defect density, and stability in halide perovskite semiconductors [21]. Feng *et al* reported the basic optical properties of a triple cation CsFAMA perovskite film and pointed out its good light absorption capabilities focusing on its employ in the inverted p–i–n solar cells [22].

Herein we investigate by means of DFT calculations the optical properties and the charge transport in two different perovskite formulations, namely the MAPI and the mixed halide (Br, I) triple cation (Cs, MA, FA) formulation triple-cation perovskite (TriLHP). We provide a theoretical calculation of the dielectric function for the TriLHP formulation and validate our approach with experimental measurements of the dielectric features of the TriLHP obtained via ellipsometry. To the best of our knowledge, a joint theoretical and experimental characterization of the dielectric properties of TriLHP has never been yet reported in literature. We use such calculations, together with the effective hole and electron masses, to give an estimate of the excitons' features in the two materials and rationalize the results in terms of their structure and composition. Our results provide an original and novel atomistic perspective on the comparative optical and charge transport features for two of the currently most used perovskite materials in photovoltaics.

## 2. Computational models

The bulk structures of both triLHP and MAPI contain 100 formula units (f.u.) and have been built by resizing the $Cs_8FA_{88}MA_{12}Pb_{103}Cd_5I_{269}Br_{55}$ supercell (108 f.u.) reported by Saidaminov [23] where Cd sites have been replaced by Pb. For both compositions 'A' and 'X' sites have been properly substituted to obtain the desired stoichiometry, namely, $MA_{100}Pb_{100}I_{300}$ and $Cs_5FA_{79}MA_{16}Pb_{100}I_{250}Br_{50}$, also employed in a previous work [8]. The structures of MAPI and TriLHP, optimized at Perdew–Burke–Erzenhof Tkatchenko–Scheffler (PBE-TS) level of theory, are shown in figures 1(a) and (b), respectively.

The two models correspond to a $5 \times 4 \times 5$ supercell of the high temperature MAPI cubic phase cell. The choice to consider such a supercell is motivated by the need to reproduce the wanted stoichiometry of the TriLHP. The calculated lattice constants for the MAPI agree with other DFT works ($a = 6.29$ Å, $b = 6.23$ Å, $c = 6.37$ Å (PBEsol)) [24] In agreement with literature introduction of Cs and large FA cations increases of $\sim$1Å the lattice constants in triLHP with respect to MAPI and widens the band gap value of about 0.1 eV. The compositon of frontiers band also aligns with literature with the valence band mostly populated by halogen species and the conduction band by lead states [3, 25].

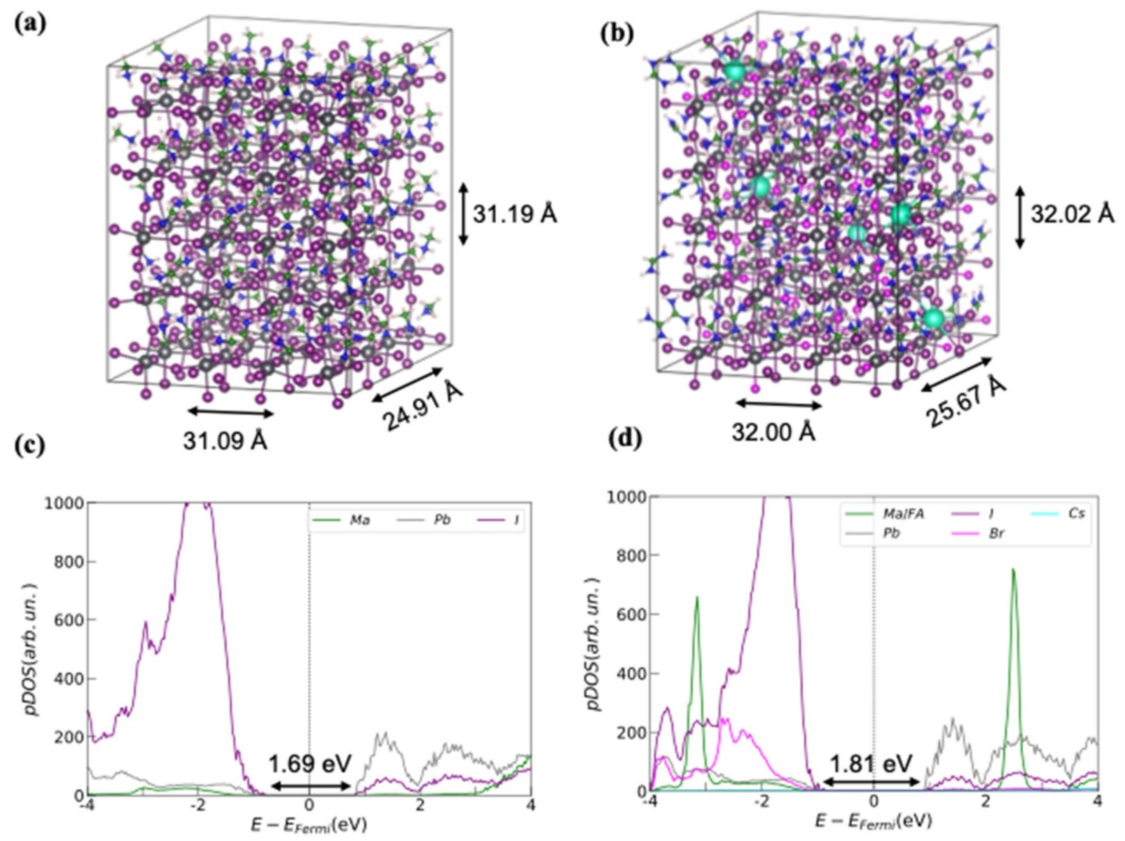

**Figure 1.** Bulk structures of the MAPI (a) and the TriLHP (b) optimized at PBE-TS level of theory. The calculated lattice constants are reported in both figures. Panels (c) and (d) report the MAPI and the TriLHP density of states projected onto atoms/moieties (MA, FA), respectively (*p*DOS). The bandgaps obtained for the two structures at PBE level of theory are reported in the *p*DOS pictures. Color legend: Cs, turquoise; N, dark blue; H, pink; C, green; Pb, dark gray; I, purple; Br, fuchsia.

## 3. Results and discussion

### 3.1. Dielectric and optical properties

The optical characteristics of solids are fundamental to optoelectronic applications such as photovoltaics [26]. Progress in this technology hinges on a comprehensive understanding of the energy dispersion of photons and associated optical parameters. We compute the macroscopic dielectric function in the visible range using the random phase approximation (RPA), while neglecting local field effects. The real ($\varepsilon_1 = \mathrm{Re}(\varepsilon)$) and imaginary ($\varepsilon_2 = \mathrm{Im}(\varepsilon)$) parts of the dielectric function ε describe the material's polarization response and its tendency for energy dissipation when exposed to incident light. Maintaining causality demands that the system's response functions adhere to the Kramers–Kronig relations. In figure 2(a), we present the real and imaginary parts of the dielectric function for the two studied compounds, calculated theoretically, while figure 2(d) shows the corresponding experimental measurements obtained via ellipsometry. The dielectric function values for MAPI are taken from the work by Manzoor *et al* [27] whereas the data for TriLHP are measured in this study. Detailed experimental procedures for the ellipsometry measurements on TriLHP are provided in the '**Experimental section**'. The calculated behavior for MAPI aligns well with other works employing RPA on top of DFT-LDA calculations [28–30].

The theoretical (a) and experimental (d) dielectric functions for both MAPI and the TriLHP show qualitative agreement in terms of the general trends, such as the position and shape of the peaks in both the real and imaginary parts. The slight shift between the theoretical and the experimental data is probably due to limitations in RPA, which does not include excitonic effects or more complex many-body interactions. The amplitudes of the peaks in the theoretical data are generally higher than in the experimental data, which may be attributed to experimental imperfections, material quality, or approximations in the theoretical model. However, despite these differences, the overall shapes and trends are consistent, suggesting that the theoretical and experimental results are reasonably in agreement, but with expected deviations due to the approximations in theory and experimental uncertainties. We also calculate the refractive indices ($n$) of the two materials that are shown in figure 2(b) while figure 2(e) displays the corresponding quantities measured experimentally. $n$ represents the real part of the complex refractive index $\tilde{n} = n + ik$ and quantifies the ratio

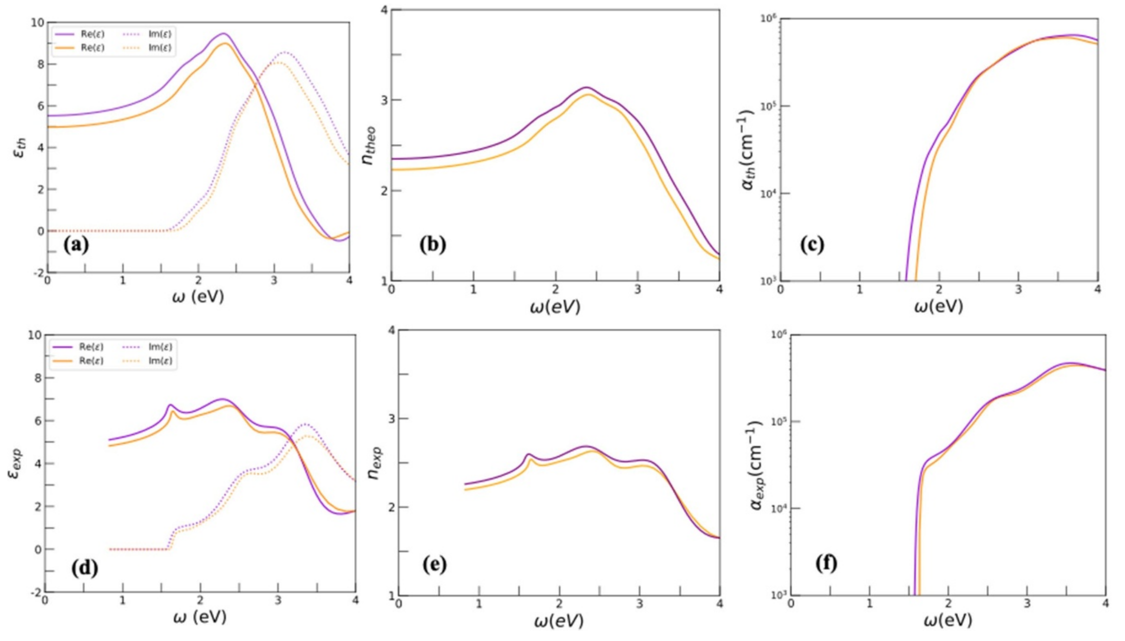

**Figure 2.** Real (solid line) and imaginary part (dotted line) of the dielectric function of MAPI (violet) and TriLHP (orange), calculated within the RPA at DFT-PBE level of theory (a). Real (solid line) and imaginary part (dotted line) of the dielectric function of MAPI (violet) and TriLHP (orange), taken from [27] and measured via ellipsometry, respectively (d). Theoretical (b) and experimental (e) refractive indices of MAPI (violet) and TriLHP (orange). Theoretical (c) and experimental (f) absorption coefficients of MAPI (violet) and TriLHP (orange).

of the speed of light in a vacuum to the phase velocity of light in the medium, thereby characterizing the extent to which the medium decelerates electromagnetic wave propagation relative to vacuum. The real and the imaginary parts of the dielectric function are related to the real and the imaginary part of the refractive index through the following relations:

$$\epsilon_1 = n^2 - k^2 \tag{1}$$

$$\epsilon_2 = 2nk \tag{2}$$

where $k$ is the extinction coefficient and characterizes the rate at which the light intensity decays due to absorption and scattering within the medium. We provide a plot of the calculated extinction coefficient in figure S1 of the Supporting Information together with a computational estimate of the dielectric loss function, figure S2. Similarly to the dielectric function, the overall behavior and the static value align well with experimental observations; however, the absence of distinct peaks are probably due to the overlooking of the excitonic effects. Theoretical and experimental absorption coefficients for both compositions are displayed in figures 2(c) and (f), respectively. Absorption coefficient ($\alpha$) is related to the imaginary parts of the dielectric function through the relation:

$$\alpha = \frac{2\omega k}{c} \tag{3}$$

where $c$ is the speed of light in vacuum and $k$ the extinction coefficient. Both calculated and measured datasets exhibit a steep increase in absorption around the band-edge region, corresponding to the onset of significant optical transitions. A slight blue shift of the absorption onset is observed in the experimental data, likely due to the slight discrepancy in the experimental and theoretical values of the bandgaps. Notably the absorption onset, is sensitive to both the kind and value used for the smearing in the calculation of the dielectric properties as also pointed out by other works.

A comparison between the two perovskite formulations reveals a stronger dielectric response for MAPI compared to TriLHP, as indicated by the higher peak intensity in the real part of the dielectric function (the static values for the two materials are $\varepsilon_{\mathrm{MAPI}} = 5.51$ and $\varepsilon_{\mathrm{TriLHP}} = 4.47$). The lower polarizability observed for the triple cation formulation is likely due to the presence of Cs that dilutes the effect of the more polarizable FA and MA cations, leading to a lower net dielectric response. Examining the imaginary part, the larger and more pronounced peak observed for MAPI suggests stronger absorption and more efficient light harvesting across a broader range of wavelengths compared to TriLHP.

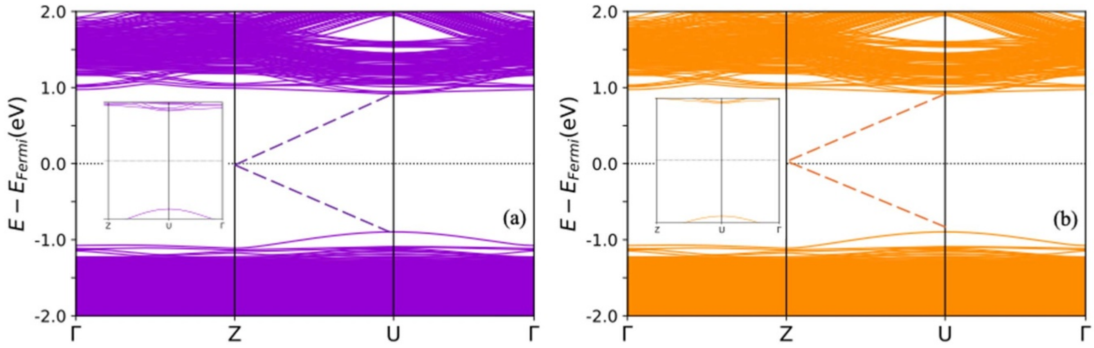

**Figure 3.** Band structures of MAPI (a) and TriLHP (b) perovskites calculated at DFT-PBE level of theory. The inset represents a magnification in the region of the bandgap transition occurring for both compounds in the U high symmetry point of the Brillouin zone.

**Table 1.** Effective hole and electron masses calculated via a parabolic fitting of valence and conduction bands, at the direct electronic transition point U, calculated at PBE level of theory. Electron–hole pair reduced mass ($\mu$), exciton binding energy ($E_b$) and radius ($R_b$) calculated using relations (4) (6) and (6). Masses are expressed as multiple of the electron rest mass $m_0$. Other studies on the MAPI formulation are included for comparison, highlighting the phase explored and the level of theory used.

| | $m_h$ ($m_0$) | $m_e$ ($m_0$) | $\mu$ ($m_0$) | $E_b$ (meV) | $R_b$ (Å) |
|---|---|---|---|---|---|
| MAPI | 0.23 | 0.23 | 0.11(5) | 51.23 | 25.42 |
| TriLHP | 0.26 | 0.19 | 0.10(9) | 60.62 | 23.92 |
| | | | Other works on MAPI | | |
| Orthorhombic [28] | 0.26 (PBE) | 0.22 (PBE) | — | — | — |
| Cubic [29] | 0.36 (PBE) | 0.32 (PBE) | 0.099 (HSE + SO) | 48 (HSE + SO) | 28 (HSE + SO) |
| Cubic [30] | 0.25,0.20,0.38 (PBE) | — | — | — | — |

### 3.2. Transport properties

We calculate the band structures of the MAPI and TriLHP formulations, to gain insights into the electron and hole transport. The corresponding band structures in the region of interest are shown in figure 3. A slightly wider bandgap is observed for mixed cation formulation (1.69 eV for MAPI and 1.81 eV for TriLHP), in agreement with literature, with both compounds displaying a direct electronic transition at the U high symmetry point of the Brillouin zone. We employ the parabolic approximation, to calculate the effective mass (m) of carriers around the conduction band minimum and the valence band maximum by fitting the dispersion relation, $E(k) = \hbar^2 k^2/2m$ where $E(k)$ is the band-edge eigenvalue and $k$ is the wavevector. The curvature of these bands determines the effective masses: a more sharply curved band corresponds to a lighter effective mass, while a flatter curve corresponds to a heavier mass.

Obtained values expressed as a multiple of the electron rest mass $m_0$, are reported in table 1.

Our results on MAPI, fairly well agree with those reported in theoretical literature even if the comparison is sometimes less direct, due to the variety of both theoretical frameworks and different phases explored [28–30]. No comparison is found for the less explored triple cation formulation. First, we can observe a perfect ambipolar conduction character of the charge transport for MAPI in which hole and electrons have the same effective masses. A more imbalanced situation is observed in the TriLHP cation formulation where electron transport seems to be slightly favored. However, the difference is small enough that both carriers still play a significant role, albeit slightly imbalanced. The lighter electron effective mass in the TriLHP can be ascribed to the structural distortions and bond length variations introduced by bromine substitution. In figure 4 are represented the pair distribution functions (PDF) for Pb-I distances in MAPI and the average Pb-X (X = I,Br) distances in TriLHP. The PDF for MAPI shows a sharp peak around 3.20 Å, indicating well-defined Pb-I distances. The representative octahedron confirms a nearly symmetric coordination environment for Pb, with bond lengths varying minimally (3.11 Å to 3.20 Å). The corresponding PDF for TriLHP shows a broader distribution, indicating an increased deviation from the mean values due to the mixed halide environment. The distances reported in the octahedron diagram show significant variations, with Pb-I bonds around 3.20 Å and Pb–Br bonds as short as 2.94 Å. Such shorter values are within the expected range in halide perovskites and do not compromise the structural stability [31]. This asymmetry reflects the different bond lengths and electronegativities of iodine and bromine. The higher electronegativity of bromine causes a shortening of the Pb-X distances that enhances orbital overlap between

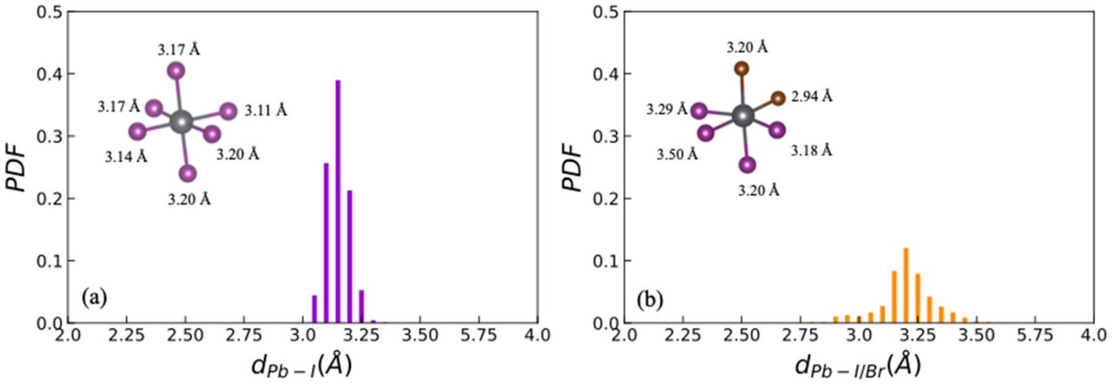

**Figure 4.** Pair distribution functions (PDF) of the Pb-I distances in MAPI (a) and the average Pb-X (X = I,Br) distances in TriLHP (b). Representative octahedra for both compositions with the corresponding metal–halogen distances reported in Å. Color legend: Pb, gray; I, violet; Br, brown.

the Pb 6p states and the Br 4p states. These states represent the main contribution to the conduction band of TriLHP and their increased overlap strengthens the hybridization of these orbitals, leading to sharper energy bands and in turn to lighter carrier masses.

We use the calculated hole and electron effective masses to calculate the hole-electron pair reduced mass, as:

$$\frac{1}{\mu} = \frac{1}{m_\mathrm{e}} + \frac{1}{m_\mathrm{h}}. \tag{4}$$

And provide an estimate of the exciton binding energy. According to the Wannier–Mott exciton model [32] the binding energy can be calculated as:

$$E_\mathrm{b} = \frac{R_\mathrm{y} m_\mathrm{e} m_\mathrm{h}}{m_\mathrm{o}\left(m_\mathrm{e} + m_\mathrm{h}\right)\varepsilon^2}. \tag{5}$$

With $\varepsilon$ and $R_\mathrm{y}$ being the dielectric and Rydberg constant, respectively. The corresponding Bohr radius is:

$$R_\mathrm{b} = \frac{\varepsilon a_0}{\mu m_0}. \tag{6}$$

To calculate exciton's properties, we use the high-frequency dielectric constant, which excludes contributions from ionic polarizabilities, thus underestimating the full dielectric response. However, our results should be interpreted as describing the exciton immediately after photoexcitation, before atomic relaxation occurs. This approach provides a qualitative upper limit for the exciton binding energy and a lower limit for the exciton radius, enabling a meaningful comparison between the two perovskite formulations.

Calculated values are reported for both formulations in table 1. The very low values obtained in both cases suggest that excitons can be instantaneously dissociated into free electrons and holes under sunlight. The value we find for MAPI agrees qualitatively with other theoretical [28] and experimental studies [33–36]. The higher value found for TriLHP is due to the lower dielectric screening, which contributes to more localized exciton formation. In both cases, the low exciton binding energy and delocalization over several lattice constants suggest that, even for the TriLHP, a more pronounced inorganic behavior is expected with respect to charge transport.

## 4. Conclusions

We report a first-principles investigation of the optical and transport properties of two of the most employed perovskite formulations in PSCs. The reliability of our theoretical results for the dielectric function in the optical regime is supported by both literature and ellipsometry measurements that we conducted for the TriLHP. The overall shapes and trends show reasonable agreement between the theoretical and experimental results, with expected deviations due to theoretical approximations and experimental uncertainties. This enables us to use our findings to compare the dielectric responses of the two materials.

Our results predict weaker dielectric screening in the TriLHP, likely due to the inclusion of cesium, which introduces an inorganic contribution that dilutes the higher polarizability of the organic moieties. The high dielectric constant of MAPI suggests potentially better defect tolerance, as the higher screening can suppress the capture of charge carriers by defect states that may form during synthesis. Furthermore, MAPI exhibits a sharper absorption peak and maintains strong absorption over a broader wavelength range, making it potentially less sensitive to fluctuations in light intensity or spectral variations.

We also compare the transport properties of the two perovskites by calculating the effective masses of charge carriers. Both materials exhibit ambipolar transport characteristics due to the similarity in hole and electron masses. However, a slight imbalance in charge transport is observed for TriLHP, where the electron effective mass is found to be lighter. A possible explanation for this difference is the influence of halogen mixing on the electronic structure. The incorporation of Br leads to shorter Pb–Br bond lengths compared to Pb-I, which may suggest a more covalent character and stronger orbital hybridization. This increased hybridization could, in turn, modify the conduction band dispersion, potentially contributing to the reduction of the electron effective mass.

Finally, we provide an estimate of the exciton's key properties, including its binding energy and radius. From an application standpoint, the exciton binding energy is critical for determining device operation, as its comparison with thermal energy ($k_B T = 25$ meV at 300 K) dictates whether photogenerated carriers behave as free carriers. The obtained values are consistent with this scenario for both formulations. Additionally, the high exciton radius, spanning several lattice constants, aligns with the characteristics of Wannier–Mott excitons, typical of inorganic materials, for both materials.

In conclusion, our results suggest that MAPI outperforms TriLHP in terms of optical and transport properties. While our findings appear to contrast with the superior experimental performance of TriLHP, this discrepancy arises because the mixed composition benefits from the superior thermal and structural stability of TriLHPs, which likely contributes to its better experimental results and greater durability under operational conditions. Our study, however, focuses exclusively on the electro-optical properties and does not consider the enhanced stability that may contribute to the overall performance of TriLHP in real-world conditions.

## 5. Experimental section

Thin films of TriLHP were fabricated on glass substrates for SE measurements. The substrates were first cleaned by sonication with acetone and ethanol and treated with UV-ozone. Triple-cation double-anion perovskite films, with composition close to $Cs_{0.05}(FA_{0.83}MA_{0.17})_{0.95}Pb(I_{0.83}Br_{0.17})_3$, were then deposited on glass via spin-coating with a one-step anti-solvent process in nitrogen filled glove box. More details can be found in [37].

SE measurements were performed with a variable angle instrument (VASE, J.A. Woollam Co., Lincoln, NE, USA), acquiring data in the range 300–1500 nm, over three angles of incidence (50°, 60°, 70°) complemented with transmittance spectra measured on the same spot. The spectra of real and imaginary part of the dielectric function (or equivalently, of the optical constants n and k—refractive index and extinction coefficient) were obtained through simultaneous fitting of the multi-angle SE data and the transmittance data with the J.A. Woollam WVASE32 software using an optical model consisting of glass-substrate/perovskite/surface-roughness-layer. The roughness layer was modelled with a 50:50 vol% mixture of the bulk layer (here the TriLHP) and voids by applying the Bruggeman effective-medium approximation. A dispersion law with multiple Tauc–Lorentz oscillators was used for the TriLHP bulk [38]. The absorption coefficient was extracted after the SE analysis as $\alpha = 4\pi k/\lambda$, where k is the extinction coefficient and λ is the wavelength.

## 6. Computational details

We performed DFT [39] calculations with periodic boundary conditions employing the light—tier1 basis set of numerical atom-centered orbitals for each atom [40] for geometry optimization and electronic analysis, respectively, as implemented in the Fritz Haber Institute *ab initio* molecular simulations (FHI-aims) code [41]. In the all-electron approach within FHI-aims framework, the electrons were described by the zero–order regular approximation (atomic ZORA) [42]. We used the PBE [43, 44] exchange correlation functional for all geometry optimizations including the TS correction [45] to account for van der Waals dispersion forces. Geometry optimizations have been carried out in the Γ point of the Brillouin zone setting a threshold for the maximum force acting on atoms equal to 0.02 eV $Å^{-1}$. Electronic structure calculations (pDOS and band structures) have been performed at PBE-TS level of theory using a $2 \times 3 \times 2$ *k*-point mesh. As self-consistency threshold for electron density convergence, we employed a total energy criterion of $1 \times 10^{-6}$ eV. Dielectric and optical properties have been calculated using the RPA on top of DFT-PBE calculations.

## Data availability statement

All data that support the findings of this study are included within the article (and any supplementary files).

## Acknowledgments

We acknowledge the support of MASE (Ministero dell'Ambiente e della Sicurezza Energetica) in the framework of the Operating Agreement with ENEA for Research on the Electric System.

We acknowledge the VIPERLAB financial support from the European Union's Horizon 2020 research and innovation programme (Grant N° 101006715).

The computing resources and the related technical support used for this work have been provided by CRESCO/ENEAGRID High-Performance Computing infrastructure and its staff [46]. CRESCO/ENEAGRID High-Performance Computing infrastructure is funded by ENEA, the Italian National Agency for New Technologies, Energy and Sustainable Economic Development, and by Italian and European research projects, see www.cresco.enea.it/english for information. The authors acknowledge the extensive use of the ENEA FARO facility and the support of its management team [47].

We also acknowledge the PRIN 2022 PNRR (P202253ANE) "Boosting CO2 conversion with Multilayer Bifunctional photoCatalysis" (BOMBCAT) for funding.

## ORCID iDs

Adriana Pecoraro https://orcid.org/0000-0002-1161-4388
Francesca Fasulo https://orcid.org/0000-0001-9008-6044
Carmen Serpico https://orcid.org/0009-0006-9473-3900
Gennaro V Sannino https://orcid.org/0000-0002-7810-1931
Lucia V Mercaldo https://orcid.org/0000-0002-7286-5236
Paola Delli Veneri https://orcid.org/0000-0002-5263-2005
Michele Pavone https://orcid.org/0000-0001-7549-631X
Ana Belén Muñoz-García https://orcid.org/0000-0002-9940-7358

## References

[1] Yang C, Hu W, Liu J, Han C, Gao Q, Mei A, Zhou Y, Guo F and Han H 2024 Achievements, challenges, and future prospects for industrialization of perovskite solar cells *Light Sci. Appl.* **13** 227

[2] Elangovan N K, Kannadasan R, Beenarani B B, Alsharif M H, Kim M-K and Hasan Inamul Z 2024 Recent developments in perovskite materials, fabrication techniques, band gap engineering, and the stability of perovskite solar cells *Energy Rep.* **11** 1171–90

[3] Saliba M *et al* 2016 Cesium-containing triple cation perovskite solar cells: improved stability, reproducibility and high efficiency *Energy Environ. Sci.* **9** 1989–97

[4] Sannino G V, Pecoraro A, Maddalena P, Bruno A, Veneri P D, Pavone M and Muñoz-García A B 2023 The role of Mg dopant concentration in tuning the performance of the $SnO_2$ electron transport layer in perovskite solar cells *Sustain. Energy Fuels* **7** 4855–63

[5] Pecoraro A, Maddalena P, Pavone M and Muñoz García A B 2022 First-principles study of cu-based inorganic hole transport materials for solar cell applications *Materials* **15** 5703

[6] Pecoraro A, Maria A D, Veneri P D, Pavone M and Muñoz-García A B 2020 Interfacial electronic features in methyl-ammonium lead iodide and p-type oxide heterostructures: new insights for inverted perovskite solar cells *Phys. Chem. Chem. Phys.* **22** 28401–13

[7] Coppola C, Pecoraro A, Muñoz-García A B, Infantino R, Dessì A, Reginato G, Basosi R, Sinicropi A and Pavone M 2022 Electronic structure and interfacial features of triphenylamine- and phenothiazine-based hole transport materials for methylammonium lead iodide perovskite solar cells *Phys. Chem. Chem. Phys.* **24** 14993–5002

[8] Pecoraro A, Fasulo F, Pavone M and Muñoz-García A B 2023 First-principles study of interfacial features and charge dynamics between spiro-MeOTAD and photoactive lead halide perovskites *Chem. Commun.* **59** 5055–8

[9] Zhou J *et al* 2024 Highly efficient and stable perovskite solar cells via a multifunctional hole transporting material *Joule* **8** 1691–706

[10] Krishna B G, Ghosh D S and Tiwari S 2023 Hole and electron transport materials: a review on recent progress in organic charge transport materials for efficient, stable, and scalable perovskite solar cells *Chem. Inorg. Mater.* **1** 100026

[11] Li S, Cao Y-L, Li W-H and Bo Z-S 2021 A brief review of hole transporting materials commonly used in perovskite solar cells *Rare Met.* **40** 2712–29

[12] Goldschmidt V M 1926 Die gesetze der krystallochemie *Naturwissenschaften* **14** 477–85

[13] Rosales B A, Hanrahan M P, Boote B W, Rossini A J, Smith E A and Vela J 2017 Lead halide perovskites: challenges and opportunities in advanced synthesis and spectroscopy *ACS Energy Lett.* **2** 906–14

[14] Abate A 2023 Stable tin-based perovskite solar cells *ACS Energy Lett.* **8** 1896–9

[15] Adinolfi V, Peng W, Walters G, Bakr O M and Sargent E H 2018 The electrical and optical properties of organometal halide perovskites relevant to optoelectronic performance *Adv. Mater.* **30** 1700764

[16] Löper P, Stuckelberger M, Niesen B, Werner J, Filipič M, Moon S-J, Yum J-H, Topič M, De Wolf S and Ballif C 2015 Complex refractive index spectra of $CH_3NH_3PbI_3$ perovskite thin films determined by spectroscopic ellipsometry and spectrophotometry *J. Phys. Chem. Lett.* **6** 66–71

[17] Hoque M N F, Yang M, Li Z, Islam N, Pan X, Zhu K and Fan Z 2016 Polarization and dielectric study of methylammonium lead iodide thin film to reveal its nonferroelectric nature under solar cell operating conditions *ACS Energy Lett.* **1** 142–9

[18] Besra N, Sardar K, Mazumder N, Bhattacharjee S, Das A, Das B, Sarkar S and Chattopadhyay K K 2021 $CH_3NH_3PbI_3$ as a radio frequency decoupling capacitor: interplay between Maxwell–Wagner polarization and a pseudo inductive response *J. Appl. Phys.* **54** 175105

[19] Srikanth M, Ozório M S and Silva J L F D 2020 Optical and dielectric properties of lead perovskite and iodoplumbate complexes: an *ab initio* study *Phys. Chem. Chem. Phys.* **22** 18423–34

[20] Leguy A M A *et al* 2016 Experimental and theoretical optical properties of methylammonium lead halide perovskites *Nanoscale* **8** 6317–27

[21] Hossain K, Singh S and Kabra D 2022 Role of monovalent cations in the dielectric relaxation processes in hybrid metal halide perovskite solar cells *ACS Appl. Energy Mater.* **5** 3689–97

[22] Feng Y, Zhang Y, Duan C, Zhao M and Dai J 2022 Optical properties of CsFAMA-based perovskite film and its application in the inverted solar cells with poly(methyl methacrylate) passivation layer *Opt. Mater. Express* **12** 3262–72

[23] Saidaminov M I *et al* 2018 Suppression of atomic vacancies via incorporation of isovalent small ions to increase the stability of halide perovskite solar cells in ambient air *Nat. Energy* **3** 648–54

[24] Brivio F, Frost J M, Skelton J M, Jackson A J, Weber O J, Weller M T, Goñi A R, Leguy A M A, Barnes P R F and Walsh A 2015 Lattice dynamics and vibrational spectra of the orthorhombic, tetragonal, and cubic phases of methylammonium lead iodide *Phys. Rev.* B **92** 144308

[25] Xu J *et al* 2020 Triple-halide wide–band gap perovskites with suppressed phase segregation for efficient tandems *Science* **367** 1097–104

[26] Bhattacharjee S, Banerjee A and Chattopadhyay K K 2024 Comparative first principles investigation on the structural, optoelectronic and vibrational properties of strain-engineered graphene-like $AlC_3$, $BC_3$ and $C_3N$ monolayers *J. Phys.: Condens. Matter* **36** 265701

[27] Manzoor S, Häusele J, Bush K A, Palmstrom A F, Carpenter J, Yu Z J, Bent S F, Mcgehee M D and Holman Z C 2018 Optical modeling of wide-bandgap perovskite and perovskite/silicon tandem solar cells using complex refractive indices for arbitrary-bandgap perovskite absorbers *Opt. Express* **26** 27441–60

[28] Menéndez-Proupin E, Palacios P, Wahnón P and Conesa J C 2014 Self-consistent relativistic band structure of the C $H_3NH_3PbI_3$ perovskite *Phys. Rev.* B **90** 045207

[29] Giorgi G, Fujisawa J-I, Segawa H and Yamashita K 2013 Small photocarrier effective masses featuring ambipolar transport in methylammonium lead iodide perovskite: a density functional analysis *J. Phys. Chem. Lett.* **4** 4213–6

[30] Yang J-P *et al* 2018 Band dispersion and hole effective mass of methylammonium lead iodide perovskite *Sol. RRL* **2** 1800132

[31] You Q, Gu S and Gou X 2023 The highly accurate interatomic potential of $CsPbBr_3$ perovskite with temperature dependence on the structure and thermal properties *Materials* **16** 2043

[32] Knox R S Introduction to exciton physics (Springer) (https://doi.org/10.1007/978-1-4684-8878-4_5) (Accessed 2 November 2024)

[33] Tanaka K, Takahashi T, Ban T, Kondo T, Uchida K and Miura N 2003 Comparative study on the excitons in lead-halide-based perovskite-type crystals $CH_3NH_3PbBr_3$ $CH_3NH_3PbI_3$ *Solid State Commun.* **127** 619–23

[34] Hirasawa M, Ishihara T and Goto T 1994 Exciton features in 0-, 2-, and 3-dimensional networks of [PbI6]4- octahedra *J. Phys. Soc. Japan* **63** 3870–9

[35] Hirasawa M, Ishihara T, Goto T, Uchida K and Miura N 1994 Magnetoabsorption of the lowest exciton in perovskite-type compound (CH3NH3)PbI3 *Physica* B **201** 427–30

[36] Ishihara T 1994 Optical properties of PbI-based perovskite structures *J. Lumin.* **60–61** 269–74

[37] Mercaldo L V *et al* 2022 Procedure based on external quantum efficiency for reliable characterization of perovskite solar cells *Energy Technol.* **10** 2200748

[38] Shirayama M *et al* 2016 Optical transitions in hybrid perovskite solar cells: ellipsometry, density functional theory, and quantum efficiency analyses for $CH_3NH_3PbI_3$ *Phys. Rev. Appl.* **5** 014012

[39] Burke K 2012 Perspective on density functional theory *J. Chem. Phys.* **136** 150901

[40] Havu V, Blum V, Havu P and Scheffler M 2009 Efficient O(N) integration for all-electron electronic structure calculation using numeric basis functions *J. Comput. Phys.* **228** 8367–79

[41] Blum V, Gehrke R, Hanke F, Havu P, Havu V, Ren X, Reuter K and Scheffler M 2009 *Ab initio* molecular simulations with numeric atom-centered orbitals *Comput. Phys. Commun.* **180** 2175–96

[42] van Lenthe E, van der Avoird A and Wormer P E S 1998 Density functional calculations of molecular hyperfine interactions in the zero order regular approximation for relativistic effects *J. Chem. Phys.* **108** 4783–96

[43] Perdew J P, Burke K and Ernzerhof M 1996 Generalized gradient approximation made simple *Phys. Rev. Lett.* **77** 3865–8

[44] Perdew J P, Burke K and Wang Y 1998 Erratum: generalized gradient approximation for the exchange-correlation hole of a many-electron system [Phys. Rev. B 54, 16 533 (1996)] *Phys. Rev.* B **57** 14999

[45] Tkatchenko A and Scheffler M 2009 Accurate molecular Van Der Waals interactions from ground-state electron density and free-atom reference data *Phys. Rev. Lett.* **102** 073005

[46] Iannone F *et al* CRESCO ENEA HPC clusters: a working example of a multifabric GPFS spectrum scale layout *Proc. 2019 Int. Conf. on High Performance Computing & Simulation (HPCS)* (*Dublin, Ireland*, *15–19 July 2019*) pp 1051–2

[47] Mariano A *et al* 2019 Fast access to remote objects 2.0 a renewed gateway to ENEAGRID distributed computing resources *Future Gener. Comput. Syst.* **94** 920–8